

Effect of Metal Doping in Bi₂WO₆ Micro-flowers for Enhanced Photoelectrochemical Water Splitting

Susmita Bera¹, Soumita Samajdar^{1,2}, Sourabh Pal¹, Pradip Sekhar Das¹, Leanne A. H. Jones³, Harry Finch³, Vinod R. Dhanak³, Srabanti Ghosh^{*1,2}

¹*Energy Materials & Devices Division, CSIR - Central Glass and Ceramic Research Institute
Raja S. C. Mullick Road, Jadavpur, Kolkata-700032*

²*Academy of Scientific & Innovative Research (AcSIR), Ghaziabad, India*

³*Stephenson Institute for Renewable Energy and Department of Physics, University of Liverpool,
Liverpool L69 7ZF, United Kingdom*

**Email: srabanti@cgcric.res.in*

Abstract:

Design and fabrication of artificial catalytic systems to mimic natural photosynthesis which can harvest solar energy and directly convert into usable or storable energy resources may resolve the global energy crisis. Remarkably, photocatalysis is an efficient approach to utilize solar photons in order to drive the thermodynamic uphill reaction to generate chemical fuels in presence of efficient photocatalyst. Bismuth tungsten oxide (Bi₂WO₆) is a typical Aurivillius double perovskite oxides photocatalyst and has received an increasing research interest for water splitting due to moderate bandgap, superior chemical and thermal stability. However, the solar light absorption of bare Bi₂WO₆ is not significant in visible region, and low charge separation efficiency limits the photocatalytic performance. In the present work, *in situ* doping of flower like Bi₂WO₆ microstructure (~6 to 8 μm) by metal (Mo, Fe, Zn) may improve the absorption and charge transfer efficiency. The metal doping effectively reduces the bandgap of Bi₂WO₆ which in turn enhances light absorption in the visible region. Notably, photoelectrochemical water splitting highly improved after metal doping, for example, Mo doping showed highest photocurrent density which is fifty-seven times higher than bare Bi₂WO₆. The band structure of Bi₂WO₆ before and after doping has been investigated on the basis of valence band XPS and Mott-Schottky analysis to understand the effect of doping in optoelectronic properties. The enhanced activity may originate due to presence of additional electronic states *via* doping, lower ionization potential, work function energy and enhanced number of charge carriers at the electrode-electrolyte interface during water splitting.

Keywords: Photocatalysis, water splitting, metal doped Bi₂WO₆, photoelectrochemical properties

1.1 Introduction

The energy generation from sustainable, reliable and affordable sources is highly desirable to address the global environmental issues and energy crisis [1-3]. Direct conversion of photon into electron to store solar energy is an elegant way for overcoming the global demands [4-6]. Photoelectrochemical (PEC) water splitting is a potential way to harvest solar energy directly by semiconductor photocatalysts and become a key technology for green H₂ generation [7-9]. Despite the worldwide attention in PEC technology, there are many parameters to explore and hurdles to overcome for reaching the viable photon to hydrogen conversion efficiency [10, 11]. The PEC efficiency can be improved by enhancing light absorption, electron-hole separation, surface charge transfer, surface kinetics and minimizing the overpotential through reducing the unwanted recombination [12-14]. Additionally, the electrode (semiconductor)-electrolyte interfaces play a decisive role in PEC performance as the photogenerated electrons and holes have to cross the junction for participating in the redox reactions [15]. Therefore, interfacial defects, nonradiative charge recombination at defect sites and alignment of energy levels are key factors which also affect the PEC performance of a photocatalyst. [12, 15, 16].

Low bandgap semiconductors have attracted considerable research focus as photo-anode/cathode in PEC water splitting due to the ability to absorb visible light (43% of the total solar spectrum) [17, 18]. In particular, the photocatalyst composed of layered semiconductors have sparked widespread interest as they can provide large active sites and structural stability by the strong chemical bonding between the layers [17, 19-23]. The Bi₂WO₆, an Aurivillius phase double perovskite oxide has attracted intense attention in photocatalysis because of its layered structure [24-26]. The crystal structure can be depicted as the alternate [Bi₂O₂]²⁺ layers stacking which are separated by [WO₆]²⁻ octahedral layers along b-axis. Previously reported studies on crystal

structure demonstrated that $[\text{Bi}_2\text{O}_2]^{2+}$ layers were composed of three different Bi(1)–O bond lengths and Bi(2)–O bond lengths, whereas WO_6 consists of six different W–O bond lengths [27]. Owing to the different bond angles and the tilting of $[\text{WO}_6]^{2-}$ octahedra, the layers are heavily distorted in the crystal lattice, which results in different order-disorder levels. In addition, the stacking of different monolayer oxides may possess oxygen depleted surfaces which gives rise to huge number of active sites [24, 27-29]. In view of active photocatalyst, Bi_2WO_6 possess higher valence band potential than that of water oxidation potential of 1.23 eV vs RHE (Reversible Hydrogen Electrode) which is advantageous for water oxidation reaction, however the moderate band gap of ~2.9 eV limits its absorption in the visible region [28-31].

Presently, doping of anion or cation in oxide-based semiconductor photocatalysts has been considered as an effective approach to expand the absorption range up to visible region by tuning the bandgap [32, 33]. The unwanted electron-hole recombination may be reduced by creating discrete energy levels near the conduction band minima (CBM) or valence band maxima (VBM), known as donor level and acceptor level, respectively [34, 35]. In addition, doping may affect the mobility of the excited electron and holes [36]. For example, Tian et al. [37] reported that Gd doping greatly influences the morphology and photocatalytic activity owing to half-filled electronic configuration of Gd^{3+} which traps the electrons and promotes charge separation efficiency. Shi et al. [38] shifted the VB of Bi_2WO_6 towards more positive potential by F^- substitution which resulted in two times higher catalytic activity for methylene blue degradation under visible light irradiation. The development of acceptor level near the VB of Bi_2WO_6 by Br doping enhanced the charge separation and migration during photocatalytic degradation of organic pollutant Rhodamine B because of the induced dipole moment by the distortion of local structure which in turn lower the band gap and decreased electronic effective mass [39]. Furthermore, Lu

[40], Ag [41], Cu [42], Zr [43], Er [44], Pt [45], Sr [46], Cd [47], La [48], and Ba [49] doped Bi_2WO_6 have been tested for organic pollutant molecules deterioration under visible light illumination. The effect of co-doping on Bi_2WO_6 has also been studied for organic pollutant degradation as it red shifted the absorption region towards longer wavelengths [50-52]. Substitution of Bi-site of Bi_2WO_6 with rare-earth ions such as Y^{3+} , Er^{3+} , Gd^{3+} and Ce^{3+} has been studied simultaneously to improve the photocatalytic activity [37, 53-56]. Hence, previous reports on doped Bi_2WO_6 photocatalysts mainly focused on organic pollutant degradation (Table S1), however the electronic factors that contribute to the photocatalytic activity and underlying mechanism are still not clear. Recently, some studies on photocatalytic H_2 generation and photoelectrochemical water splitting have been reported using metal doped Bi_2WO_6 [57-59]. For example, Etogo et al. [58] demonstrated photocatalytic O_2 evolution ($147.2 \text{ mmol h}^{-1} \text{ g}^{-1}$) using Mo-doped Bi_2WO_6 biscuit-like microstructures under visible light due to the successful reduction of bandgap from 2.9 eV to 2.47 eV. Keerthana et al. [59] selected Ni as dopant for Bi_2WO_6 due to its high conductivity, mobility and low driving potential and used as efficient electrocatalyst for O_2 evolution reaction. Very recently, Koteski et al. [60] investigated the structural, optical and electronic properties of Mo, Zn, Fe, Cr doped Bi_2WO_6 using density functional theory (DFT) and stated that Zn doping is more effective than others as it reduce the bandgap by inducing a shift near the top of VB toward higher energies.

In this work, we have partially substituted the W-site with Mo, Fe and Zn of Bi_2WO_6 and studied the effect in optical absorption and photoelectrochemical water splitting. Mo has been selected as it is isoelectric with W, which may cause minimum perturbation of the host lattice and reduce the probability of extra phase generation. Depending on the theoretical investigation, Fe and Zn have been selected to study the effect in water splitting under visible light illumination. By varying

dopant concentration, catalytic activity has been tuned. Among various doping, the 6% Mo doped Bi_2WO_6 exhibits highest photocurrent density. The origin of the enhanced photoelectrochemical performance for Mo substitution at W-site has been investigated on the basis of band structure by utilizing UV-Visible absorption, valence-band X-ray photoelectron spectroscopy (VB-XPS), Nyquist and Mott–Schottky analysis.

2. EXPERIMENTAL SECTION

2.1 Chemicals

Bismuth nitrate pentahydrate [$\text{Bi}(\text{NO}_3)_3 \cdot 5\text{H}_2\text{O}$], sodium molybdate dihydrate [$\text{Na}_2\text{MoO}_4 \cdot 2\text{H}_2\text{O}$], sodium tungstate dihydrate [$\text{Na}_2\text{WO}_4 \cdot 2\text{H}_2\text{O}$], zinc nitrate hexahydrate [$\text{Zn}(\text{NO}_3)_2 \cdot 6\text{H}_2\text{O}$], iron nitrate nonahydrate [$\text{Fe}(\text{NO}_3)_3 \cdot 9\text{H}_2\text{O}$], acetic acid, Polyvinylpyrrolidone (PVP), ethylene glycol, methanol and ethanol were obtained from Merck. Millipore System was used to get DI water (18.2 $\text{M}\Omega\cdot\text{cm}$).

2.2 Synthesis of Bi_2WO_6 flower structure

A facile hydrothermal method has been followed to synthesize assembled flower-like Bi_2WO_6 with some modification [58]. At first, 0.77 g $\text{Bi}(\text{NO}_3)_3 \cdot 5\text{H}_2\text{O}$ (0.02 M) and 1.6 g PVP were dissolved in 40 mL ethylene glycol and stirred for 15 minutes at room temperature. In another beaker, 40 mL of 0.01 M (0.26 g) Na_2WO_4 aqueous solution was prepared and then added into the $\text{Bi}(\text{NO}_3)_3$ solution dropwise with vigorous stirring. A white precipitate was formed after being stirred for extra 1 h. Finally, the suspension was transferred into a 100 mL capacity autoclave, heated at 220°C for 20 h. The resulting sample was washed by centrifugation in DI water thrice and once in

ethanol. After that, the collected sample was dried overnight in an oven at 50°C. The final powder of Bi₂WO₆ was marked as BiW.

2.3 Synthesis of the metal (Mo, Fe, Zn) doped Bi₂WO₆

To prepare Mo doped Bi₂WO₆, the stoichiometric amounts of [Bi(NO₃)₃·5H₂O], [Na₂WO₄·2H₂O], and [Na₂MoO₄·2H₂O] precursors were taken in a ratio of Bi : (W, Mo) = 2:1 and the Mo was taken as atomic percentage of 2%, 4%, 6%, 8%, and 10%. After being stirred for 1h, the suspension was transferred into a Teflon-lined autoclave, capacity 100 mL and heated at 220°C for 20 h. The resulting sample was washed by centrifugation in DI water thrice and once in ethanol. After that, the collected sample was dried overnight in an oven at 50°C. The final powder of Mo-doped Bi₂WO₆ was marked as BMW-2%, BMW-4%, BMW-6%, BMW-8%, BMW-10%. Following the similar reaction condition, Zn and Fe-doped Bi₂WO₆ have been prepared using [Zn(NO₃)₂·6H₂O] and [Fe(NO₃)₃·9H₂O] as Zn and Fe precursors, respectively. The Fe doped samples were marked as BFW-2%, BFW-4%, BFW-6%, BFW-8%, BFW-10% and Zn doped samples as BZW-2%, BZW-4%, BZW-6%, BZW-8%, BZW-10%.

2.4 Characterizations

Philips X'Pert instrument was used to study X-ray diffraction (XRD) of BiW samples before and after doping. The elemental presence and the morphology of bare semiconductors and heterojunction were recorded by field emission scanning electron microscopy (FESEM), for which Sigma (LEO. 430i) Carl-Zeiss instrument was employed. XPS was employed to measure the core-level spectra, VB DoS, and secondary electron cutoff (SEC) of the as synthesized Bi₂WO₆ and Mo doped Bi₂WO₆ materials. XPS measurements were used for Mo doped Bi₂WO₆ as it exhibited

highest photocurrent density out of the three systems studied. The measurements were performed in a standard ultrahigh vacuum chamber operating at a base pressure of less than 2×10^{-10} mbar, with H_2 as the main residual gas. The excitation source was monochromatized Al $K\alpha$ X-ray radiation, operating at 250 W. The XPS was operated at a resolution of 0.38 eV as determined from the width of the Fermi edge of a polycrystalline Ag sample. Further experimental details, including the spectrometer calibration, can be found elsewhere [61, 62]. C 1s (284.5 eV) spectrum was considered as standard for charge correction. The UV-Visible absorption spectra of the semiconductor materials were taken at room temperature by using Cary 5000 UV-VIS-NIR spectrophotometer.

2.5 Photoelectrochemical measurements

The thin films of the materials were prepared by spin coating method at rpm of 4000 and time duration 1 min (catalyst concentration: 2mg/mL) on a FTO glass of area 1 cm². In total, 300 μ L solution was used to prepare the three layers on the FTO slides and finally dried at 200°C for 2h. A potentiostat (Autolab, PGSTAT302N, The Netherlands) was employed to measure the photoelectrochemical properties of the as prepared materials. A three-electrode quartz cell having 0.1 M Na₂SO₄, KCl saturated Ag/AgCl, Pt wire were used as electrolyte, reference electrode and counter electrode, respectively. Thin film of the materials on the FTO coated glass has been taken as working electrode. The experiment was carried out under Xenon light source of 35 mW/cm² intensity. The photocurrent density of the bare BiW and doped BiW was recorded in the potential region of -0.4 V to 1V vs Ag/AgCl at scan rate of 10 mV s⁻¹ via linear sweep voltammetry (LSV). Furthermore, the light sensitivity and the stability were examined through chopped chronoamperometry (CA) at a fixed voltage of 0.26V vs Ag/AgCl. To investigate the conductivity

and electron-hole transfer resistance at the electrode-electrolyte interfaces, electrochemical impedance spectra (EIS) were taken. The frequency range for this EIS measurement was 100 KHz to 0.1 Hz and amplitude was 0.1 V. Moreover, the Mott-Schottky (M-S) study was carried out at 1000 Hz frequency to study junction capacitance at the electrode-electrolyte interface, flat band potential, free charge carrier density and conductivity of the materials. The Nernst equation was employed to convert the potentials ($E_{\text{Ag/AgCl}}$) to normal hydrogen electrode scale (E_{RHE}), as follows:

$$E_{\text{RHE}} = E_{\text{Ag/AgCl}} + 0.059 \times \text{pH} + 0.197 \quad (1)$$

3. RESULT & DISCUSSIONS

3.1 Physicochemical properties

The characteristic X-ray diffraction peaks of 28.32° , 32.89° , 47.05° , 55.90° , 58.60° , corresponding to the (113), (200), (202), (331), and (262) planes of Bi_2WO_6 , reveal that as prepared Bi_2WO_6 is highly crystalline and exists in orthorhombic phase with space group $\text{Pca}2_1$ (JCPDS no. 73-1126) [36]. The XRD pattern of the different Mo-doped Bi_2WO_6 are shown in Figure S1, where the similar diffractograms after Mo-doping suggests the isostructural nature of Mo- Bi_2WO_6 samples with pure orthorhombic Bi_2WO_6 phase [37, 38]. However, a shift of characteristic (113) peak towards larger 2θ value indicates the shrinkage of the lattice parameters of (113) plane due to the W^{6+} substitution by Mo^{6+} [36, 58]. The XRD of 6% Mo, Fe, Zn-doped BiW, presented in Figure 1, illustrates that metal substitution does not change the crystal arrangements of Bi_2WO_6 . Additionally, no other additional peaks have been observed after metal doping, which implies that metal substitution did not result in new crystal development or crystal orientations [36-38]. However, a shift in the (131) diffraction peak at the range of $2\theta = 27\text{--}30^\circ$ was observed towards a larger 2θ value, which confirms the successful W^{6+} substitution by the smaller metal ions [58].

Additionally, the shifting of 0.07° , 0.05° and 0.04° have obtained for (113) plane after partial substitution of Mo, Fe and Zn, respectively, which implies that the crystal structure of doped- Bi_2WO_6 remains in same orthorhombic phase with space group $\text{Pca}2_1$ [58]. The crystallite size, (D) of the pristine Bi_2WO_6 and metal doped Bi_2WO_6 have been calculated using the Scherrer formula of;

$$D = \frac{0.94 \lambda}{\beta \cos \theta} \quad (2)$$

where, λ is the wavelength of the X-ray beam (1.5406\AA), β is full width at half maxima (FWHM) of the highest intensity peak (radian). The crystallite size of the bare Bi_2WO_6 and 6 % metal-doped Bi_2WO_6 are calculated for the (113) characteristic plane, which are presented in Table 1. It has been clearly observed that, after metal ion substitution the crystallite size reduces and attends minimum value for 6% Mo-doping. The partial substitution of W^{6+} by Mo^{6+} may causes a lattice distortion due to different ionic radii of W and Mo and prevent the grain growth, results decrease in crystallite size. Furthermore, the corresponding strains (ε) have been evaluated as the distortion related with the strain present in the lattice, using the following equation:

$$\varepsilon = \frac{\beta}{4 \tan \theta} \quad (3)$$

As expected, the lattice stain increases after the metal ion substitution, which is well consistent with the previously reported studies (Table 1) [63-66].

Table 1 Crystallite size and lattice stain of pristine Bi_2WO_6 and metal doped (Mo, Fe, Zn)- Bi_2WO_6 .

Material	2θ	Full width at half maximum (FWHM, β)	Crystallite size (D nm)	Strain $\varepsilon \times 10^{-3}$
Bi_2WO_6	28.24	0.28	30.48	4.84
6% Mo-Bi_2WO_6	28.53	0.48	17.79	8.27
6% Fe-Bi_2WO_6	28.51	0.47	17.85	8.24
6% Zn-Bi_2WO_6	28.48	0.41	20.89	7.05

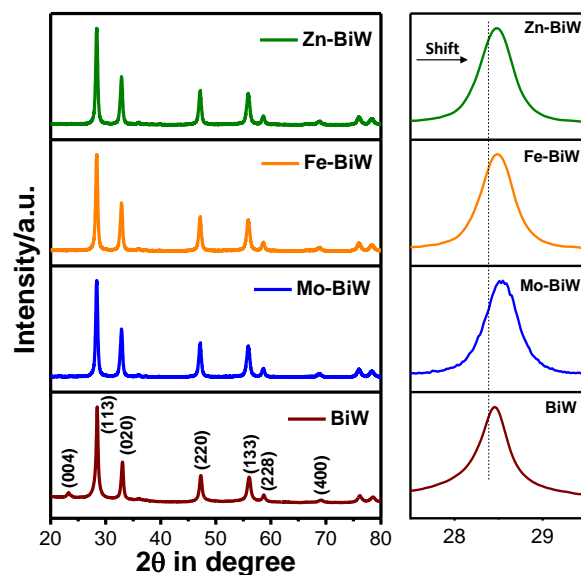


Figure 1 (a) XRD patterns of bare Bi_2WO_6 (BiW), Mo-doped Bi_2WO_6 (Mo-BiW), Fe-doped Bi_2WO_6 (Fe-BiW) and Zn-doped Bi_2WO_6 (Zn-BiW). (b) XRD patterns of the bare BiW and doped BiW in the 2θ range of $27\text{--}30^\circ$.

A flower like assembled micro-structure of average size $1.5\ \mu\text{m}$ have been obtained for BiW, which consist of building blocks of individual small nanosheets (Figure 2a). The FESEM images of doped BiW are represented in Figure 2b-d. Interestingly, Mo doping does not affect the flower like structure of BiW, however it changes after Fe and Zn doping. The energy dispersive X-ray (EDX) analysis of 6% Mo-BiW has been studied to confirm the atomic percentage of Mo doping as well as presence of elements. Figure 3a shows the EDX of 6% Mo-BiW, where peaks for Bi, W, Mo and O are present with the atomic ratio of 20.26%, 7.05%, 5.3%, 67.39%, revealing excess O in the lattice. The mapping of the individual elements clearly reveals the presence of Bi, W, O and Mo (Figure 3b-e).

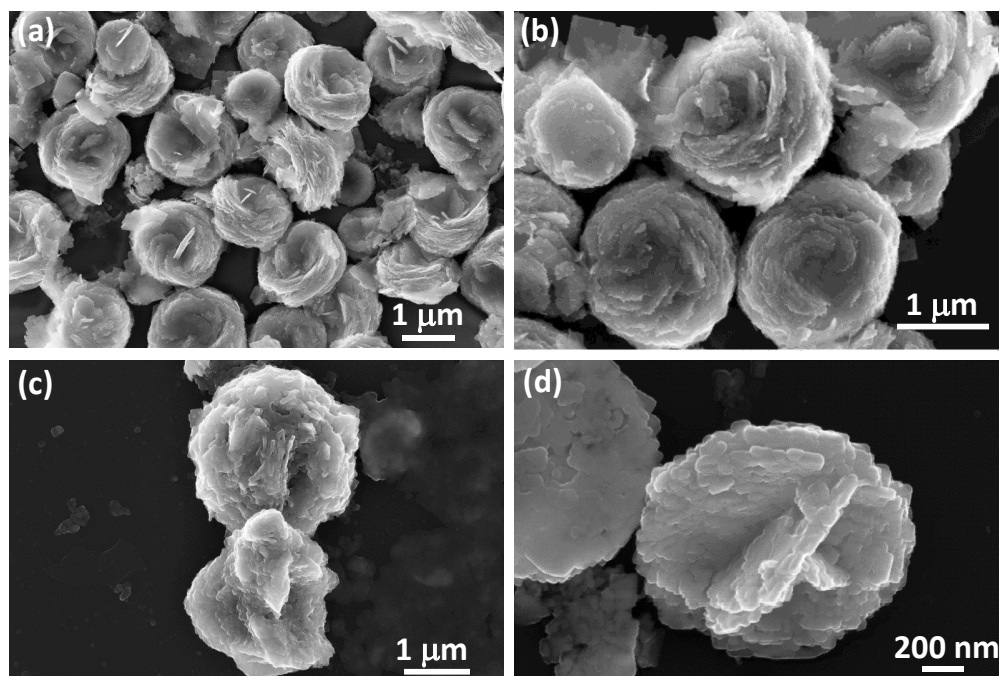


Figure 2 FESEM images of (a) bare Bi₂WO₆ (BiW), (b) Mo-doped Bi₂WO₆ (Mo-BiW), (c) Fe-doped Bi₂WO₆ (Fe-BiW) and (d) Zn-doped Bi₂WO₆ (Zn-BiW).

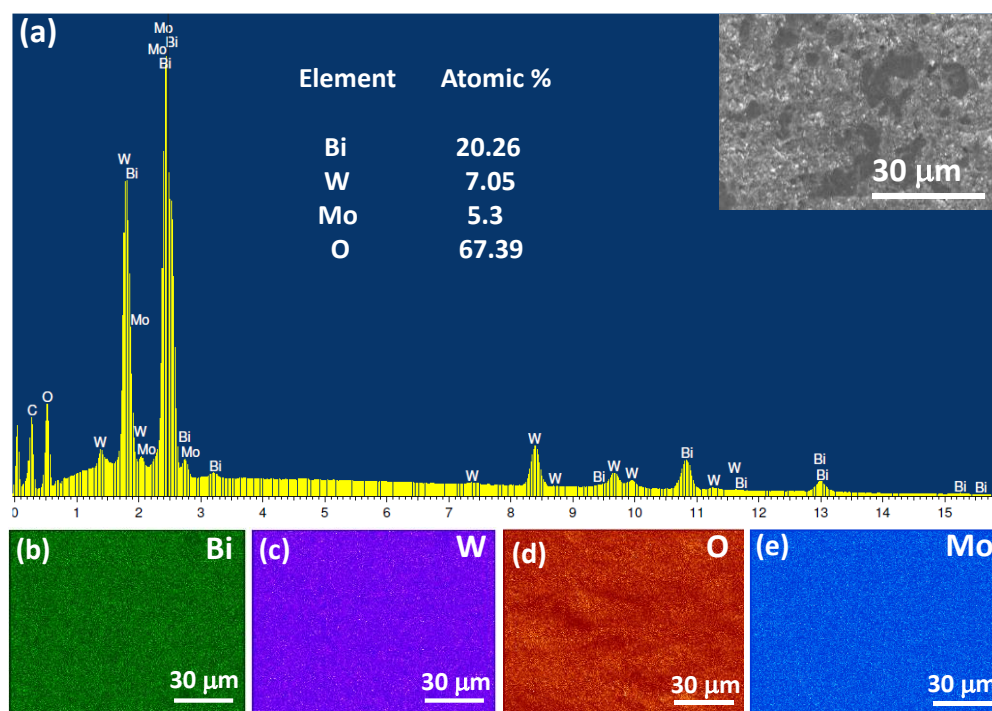


Figure 3 FESEM EDX of 6% Mo-BiW and the elemental mapping of Bi, W, O and Mo.

For better understanding the effect of Mo-doping in crystallinity of Bi_2WO_6 , TEM and high resolution TEM (HRTEM) have been carried out. Figure 4a and 4c illustrate the TEM images of pristine Bi_2WO_6 and 6 % Mo-doped Bi_2WO_6 , clearly reveal that nanosheets are stacked together and oriented in a certain direction to form flower like microstructure. The HRTEM images of Bi_2WO_6 and 6 % Mo-doped Bi_2WO_6 exhibit clear lattice fringes, indicate the highly crystalline nature of the as prepared materials. The interplanar spacing of 0.312 nm corresponds to the (113) plane of orthorhombic Bi_2WO_6 [Figure 4b and 4d] [67].

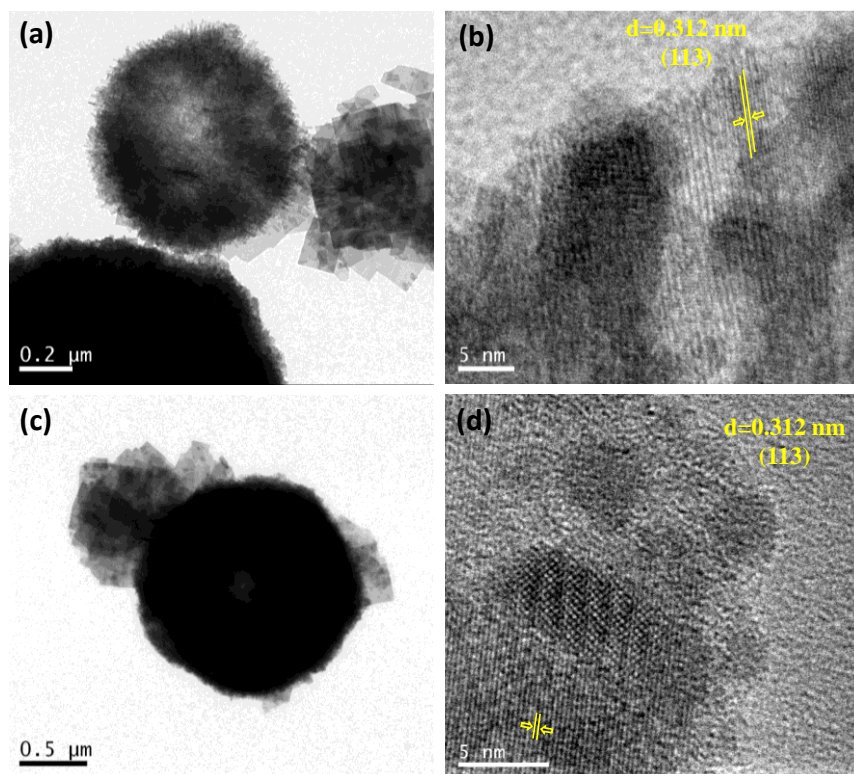


Figure 4 (a) TEM image and (b) HRTM image of Bi_2WO_6 . (c) TEM image and (d) HRTM image of Mo-doped Bi_2WO_6 .

To confirm the oxidation states and the chemical environment surrounding the elements, XPS analysis of BiW before and after Mo doping was performed. Figure S2 represents the surface

survey spectra of the bare BiW and the 6% Mo-BiW, which confirms the presence of Bi, W, O, C and Mo after doping. Further, the high-resolution spectra of the core levels were fitted using Gaussian-Lorentzian line shape analysis to determine the oxidation state of the elements. Details of the fitting procedure can be found elsewhere [62]. Figure 5a shows the Bi 4f core levels for bare BiW and 6% Mo-BiW. The Bi 4f spectra of BiW, fitted with two doublet peaks at the bonding energies of ~159.47 eV and ~164.75 eV with the spin orbit separation of 5.31 eV, corresponds to Bi 4f_{7/2} and Bi 4f_{5/2} respectively, and confirms the presence of Bi³⁺ state [68]. However, after Mo-doping, both Bi 4f_{7/2} and Bi 4f_{5/2} appear asymmetric and have been fitted with two extra peaks (Figure 5a). The additional peaks at higher binding energies may arise due to presence of Bi–O–Bi bond, i.e. during doping some Bi₂O₄ may be formed at the surface [69]. However, in XRD no additional peak were observed after Mo-doping, clearly implying that it is mainly present in the surface or subsurface region of the materials. Two characteristic peaks in the W 4f spectrum at binding energies of ~35.8 eV and ~37.95 eV with spin orbit separation of 2.14 eV, ascribed to W 4f_{7/2} and W 4f_{5/2}, respectively, confirms the presence of W⁶⁺ state [58, 59]. In addition, two small peaks at ~34.59 eV and ~36.64 eV reveal the presence of W⁵⁺ state within Bi₂WO₆ which may arise due to appearance of defect sites, i.e. oxygen-deficient W within the crystal lattice [70]. Interestingly, the W⁵⁺ state was not observed after Mo-doping at the W-site, and significantly the peak position shifted towards lower binding energies, which indicates the change of surface electron density for W after Mo substitution (Figure 5b) [36, 58]. The O1s lineshape for bare Bi₂WO₆ was fitted with three peaks at binding energies of ~530.15 eV, ~530.74 eV and ~532.4 eV, related to the lattice oxygens of W–O, Bi–O and surface adsorbed oxygen, respectively [71]. As expected, the O1s lineshape of Mo-Bi₂WO₆ was more complex and fitted with four peaks

correspond to Bi–O (~530.15 eV), W–O (~530.85 eV), Mo–O (~531.99 eV) and adsorbed O (~533.6 eV) (Figure 5c) [72].

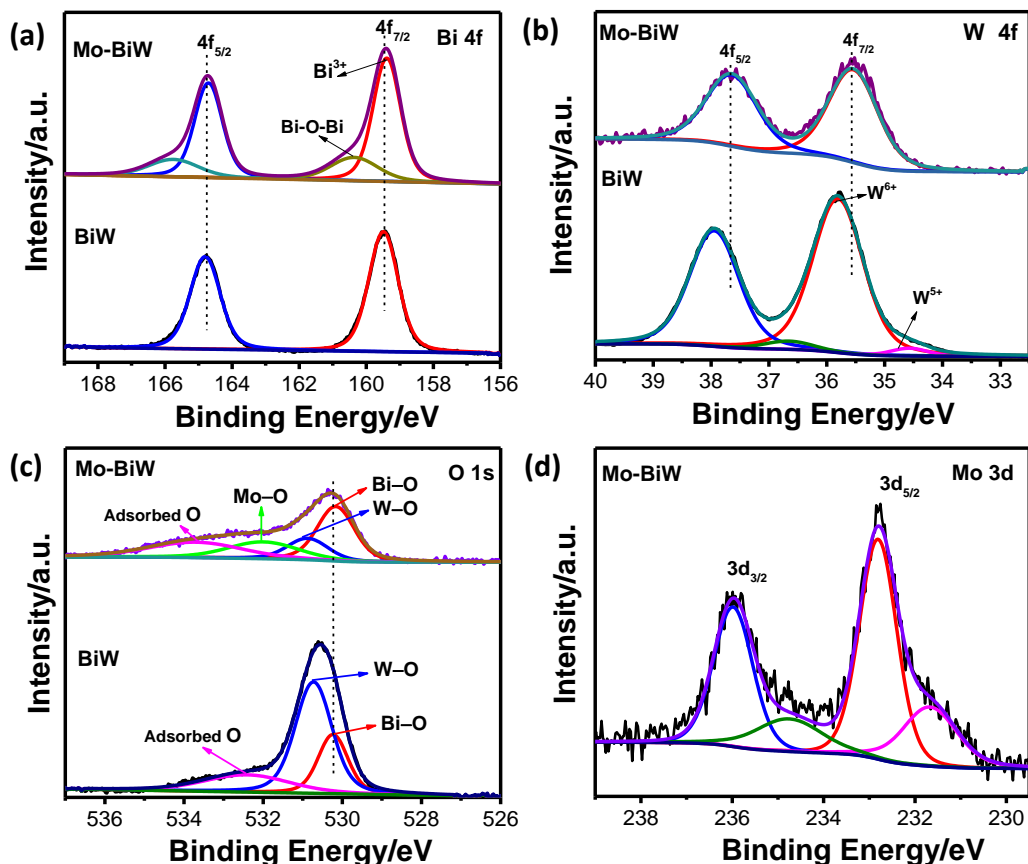


Figure 5 Core level XPS spectra of (a) Bi 4f, (b) W 4f, (c) O 1s and (d) Mo 3d of bare BiW and Mo-BiW.

The main Mo 3d peaks at ~232.7 eV and ~235.9 eV are in good agreement with Mo in the Mo⁶⁺ state (Figure 5d) [58]. Although W and Mo remains in same oxidation state (W⁶⁺ and Mo⁶⁺), slight difference in binding energy has been founded for W–O and Mo–O (Figure 5c), which may possibly for the different electronegativity of W (2.36) and Mo (2.16). It is noted that the Mo 3d lineshape has a slight asymmetry towards lower binding energies and the core level doublets have been fitted with two extra peaks to account for the asymmetry (Figure 5d) [29]. The minor peaks

centered at ~231.66 eV and ~234.7 eV are attributed to the presence of Mo^{5+} state, which are well consistent with the previously reported literatures [73, 74]. Furthermore, the FTIR analysis have been carried out for pristine BiW and metal-doped BiW to confirm the chemical bonds present in the molecules (Figure S3). The characteristic absorption band at $\sim 731 \text{ cm}^{-1}$ corresponds to W–O and Bi–O stretching vibrations, which has been reduced after metal substitution [75]. The decrease in band intensity confirms that metal doping may significantly affect the W–O and Bi–O bonds. The band at $500 \text{ to } 600 \text{ cm}^{-1}$ is related to the bridging vibration W–O–W [76]. The characteristic bands at $\sim 1625 \text{ cm}^{-1}$ and $\sim 3423 \text{ cm}^{-1}$ are ascribed to the bending and stretching vibrations of O–H bond.

The light absorption and the band gaps of the bare BiW and the 6% metal doped BiW have been studied by UV-Vis absorption spectra (Figure 6a). Bare semiconductor BiW has very low absorption in visible region due to large band gap of 2.9 eV. As expected, the light absorption ability of BiW was increased and extended to the visible region after metal doping due to the reduction of bandgap energy. The bandgap energy (E_g) of BiW and metal doped BiW are calculated using Kubelka–Munk equation of [77];

$$(\alpha h\nu) = C(h\nu - E_g)^n \quad (4)$$

Where, $h\nu$ denotes photon energy, α is linear absorption coefficient, C is proportionality constant. The value of n is related to electronic transitions of the material. The value of $n = 1/2, 3/2, 2, 3$ corresponds to direct allowed, direct forbidden, indirect allowed, and indirect forbidden electronic transition, respectively. For BiW, it is widely accepted that electronic transition is indirect allowed i.e. $n = 2$, [36, 58]. The calculated E_g values are 2.9 eV, 2.54 eV, 2.6 eV and 2.82 eV for BiW, Mo-BiW, Fe-BiW and Zn-BiW, respectively (Figure 6b). Thus, Mo-doping successfully narrowed the

E_g compared to Fe and Zn-doping, due to the hybridized conduction band of Mo 4d and W5d orbitals which may generate an impurity level below the CBM.

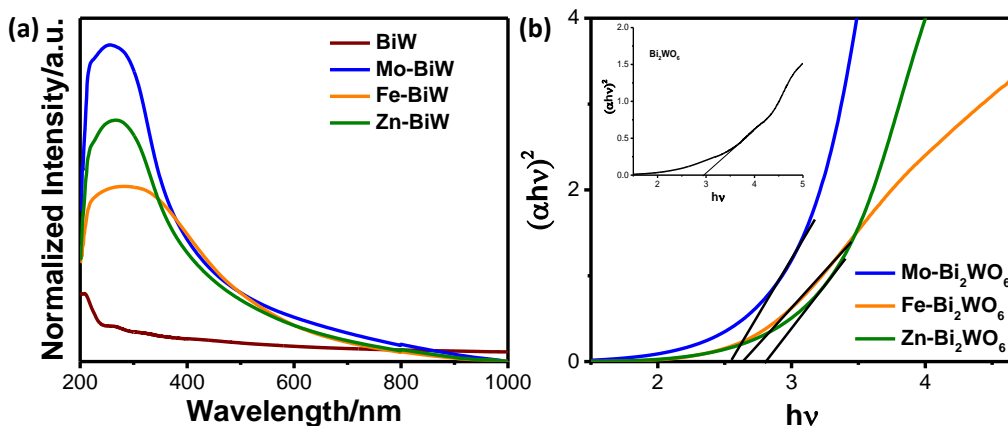


Figure 6 (a) The UV-Vis absorption spectra and corresponding (b) Kubelka–Munk $[(\alpha h\nu)^2$ vs photon energy ($h\nu$)] plots of bare BiW (Inset of Figure 6b), Mo-BiW, Fe-BiW and Zn-BiW.

The generation of extra electronic state boosts the electron excitation from the VBM to CBM and improves the light absorption by narrowing the band gap. In addition, the degree of delocalized excitation energy because of crystal structure distortion through Mo substitution may have an effect in bandgap reducing [36, 58].

3.2 Photoelectrochemical properties

Photoelectrochemical properties of the prepared thin films have been studied to check the photo-response as well as stability of material under light illumination. Figure 7(a-d) represents the linear sweep voltammetry (LSV) spectra of bare BiW and 6% metal (Mo, Fe, Zn) doped BiW under dark and light irradiation. As expected, Mo-doping effectively enhances the photocurrent density up to 0.4 mA cm^{-2} which is much higher than bare BiW ($7.07 \text{ } \mu\text{A cm}^{-2}$). Moreover, the Mo-BiW exhibits 2.3 fold and 57 fold higher current density compared to Fe-BiW (0.17 mA cm^{-2}) and Zn-BiW

($8.49 \mu\text{A cm}^{-2}$), respectively. The LSV of the as prepared materials under chopped light condition were also studied to determine the onset potential as well as the photo bleaching effect of the material. The onset potential of BiW, 6% Mo-BiW, 6% Fe-BiW and 6% Zn-BiW are -0.3 V , -0.4 V , -0.44 V and 0.15 V (vs Ag/AgCl), respectively.

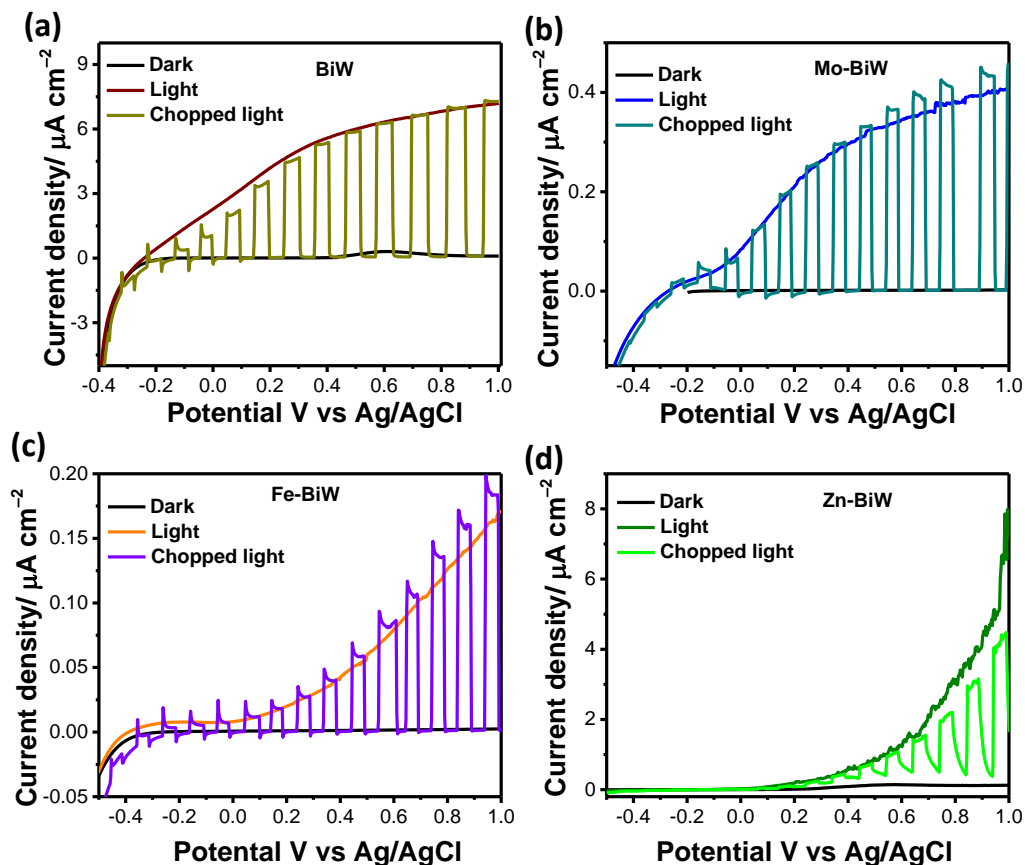


Figure 7 LSV spectra of (a) bare BiW, (b) Mo-BiW (6 % doping), (c) Fe-BiW (6 % doping) and (d) Zn-BiW (6 % doping) under dark, continuous light and chopped light illumination. The experiment was performed in a three-electrode cell, Ag/AgCl as reference electrode and Pt wire as counter electrode and 0.1 M Na_2SO_4 solution as electrolyte.

Therefore, it can be concluded that Mo and Fe substitution effectively reduces the work function energy of BiW for water splitting under visible light illumination. Furthermore, the effect of dopant

concentration in water splitting has been studied through chopped LSV for Mo-BiW materials (Figure S4). Among various dopant concentration, 6% Mo-BiW exhibits highest photocurrent response which might be attributed to the suitable amount of Mo doping and reduced bandgap, thereby allowing better visible light absorption and charge separation [58, 78]. Chronoamperometry (CA) of the prepared photoanodes has been performed to check the photo-response and stability of the materials. As shown in Figure 8a, 6% Mo-BiW represents three times higher photo current density as well as stability compared to 6% Fe-BiW. To compare the results, CA of bare BiW and 6% Zn-BiW have been studied and presented in Figure 8b. From the result, it is clear that metal-doping successfully enhances the photo-stability and reduces the photo-bleaching effect of BiW. The reusability of the photoanode has been tested by taking the linear sweep voltammetry (LSV) spectra of Mo-doped Bi_2WO_6 for five successive runs, where the photocurrent density almost remain same upto three runs (Figure S5a). Furthermore, photo bleaching effect of Mo-BiW has been studied by taking CA for 10 mins under continuous visible light illumination, where a stable current density obtained, reveals the low photobleaching effect (Figure S5b). Further, morphology of the photoanode has been checked after ten successive LSV runs to analysis the morphological change. From the Figure S5c, it can be clearly observed that assembled flower like structure are present along with some agglomeration. Thus, it can be concluded that prepared photoanode of Mo- Bi_2WO_6 is reusable and stable. To understand the origin of highest performance of Mo-doping, charge transfer resistance of the doped and undoped BiW at the electrode-electrolyte interface have been measured through electrochemical impedance spectra under visible light illumination (Figure 8c). The diameter of the semicircular arc indicates the charge transfer resistance of the photoanode material at the electrode-electrolyte interface [66]. The 6% Mo-doping results minimum charge transfer resistance of $\sim 1200\ \Omega$ than that of 6% Fe-

BiW ($\sim 9 \text{ k}\Omega$) and 6% Zn-BiW ($\sim 21 \text{ k}\Omega$), implies higher conductivity and facile charge transfer in case of Mo-doping under light illumination. Furthermore the effect of light illumination on the charge transfer resistance has been studied for 6% Mo-BiW, where charge transfer resistance significantly decreases after light illuminations (Figure S6), indicating improved activity by the photogenerated charge species. The lower charge transfer resistance and improved redox activity of Mo-BiW resulted three times higher H_2 generation rate compared to pristine Bi_2WO_6 (Figure S7).

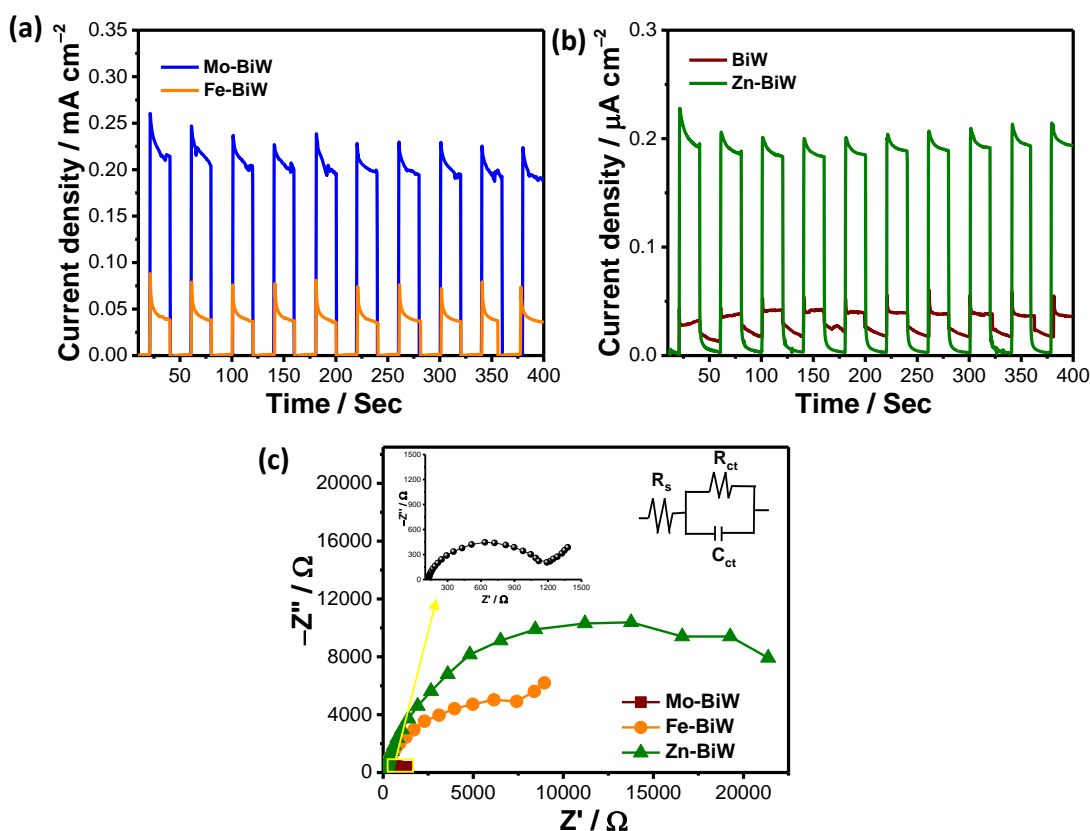


Figure 8 (a) Transient photocurrent spectra of Mo-BiW (6 % doping) and Fe-BiW (6 % doping) through chronoamperometry under chopped light condition. (b) Transient photocurrent spectra of bare BiW and Zn-BiW (6 % doping) through chronoamperometry under chopped light condition. (c) Nyquist plot of Mo-BiW (6 % doping) and Fe-BiW (6 % doping) and Zn-BW (6 % doping) at a fixed potential of 0.26 V vs Ag/AgCl in 0.1 M Na_2SO_4 electrolyte under visible light.

3.3 Mechanism

For better understanding the electronic structure and the parameters which influence the enhanced catalytic activity of Mo-BiW, junction capacitance at the electrode-electrolyte interfaces through Mott-Schottky (M-S) and valence band XPS (VB-XPS) have been studied. The M-S studies have been performed in presence of 0.1 M Na₂SO₄ electrolyte to get the information about nature of the semiconductors, determination of flat band potential (E_{fb}), number of free charge carriers and effect of doping in electronic structure. All of the materials exhibit positive slopes in M-S measurement i.e. confirm n-type conductivity (Figure 9) [80]. The flat band potentials (E_{fb}) of the materials have been calculated from the slope of $1/C^2$ vs potential plot at $1/C^2 = 0$ using the equation of [81, 82];

$$\frac{1}{C_s^2} = \frac{2}{eN_d\epsilon\epsilon_0} \left(E - E_{fb} - \frac{KT}{e} \right) \quad (5)$$

where, C_s indicates space charge capacitance at the electrode-electrolyte junction (in F cm⁻²), N_d is the free charge carrier density (in cm⁻³), e is electronic charge (in C), ϵ and ϵ_0 are dielectric constants of semiconductor and permittivity of free space, K and T are Boltzmann constant and temperature (in K), respectively. It is well known that, in case of n-type semiconductors the flat band potentials are located near the CB. Previously reported studies stated that the difference between CBM and E_{fb} , i.e. ΔE is 0.2V for conductivity in the order of 10² Ω [83]. Considering this ΔE , the conduction band minima (CBM) and valence band maxima (VBM) are calculated and presented in Table 2. The CBM potentials for BiW and Mo-BiW are -0.08 eV and -0.35 eV, respectively, thereby a shift of 0.27 eV in CBM happened due to Mo doping, which boosts the water reduction efficiency. Notably, the Fe and Zn-doping also shifted the CBM towards more negative potential. With the help of the E_g values which are determined from the Kubelka–Munk plots, the position of the VBM was further calculated [68]. The VBM of bare BiW, Mo-BiW, Fe-

BiW and Zn-BiW are 2.82 eV, 2.19 eV, 2.64 eV and 2.72 eV, respectively, therefore VBM are pushed up after metal doping. Interestingly, 6% Mo-doping narrowed the bandgap and resulted VBM position near the water oxidation potential (1.23 V vs RHE) and highly negative CBM which is suitable for water reduction (0 V vs RHE). In addition, free charge carrier concentrations of doped BiW have been calculated, where 6% Mo-BiW shows highest value ($311.5 \times 10^{16} \text{ cm}^{-3}$) than that of 6% Fe-BiW ($260.6 \times 10^{16} \text{ cm}^{-3}$), 6% Zn-BiW ($101.5 \times 10^{16} \text{ cm}^{-3}$) and bare BiW ($69.6 \times 10^{16} \text{ cm}^{-3}$). Thus, higher number of free charge carriers and the suitable oxidation and reduction potential of 6% Mo-BiW are two basic parameters for the enhanced water splitting capability.

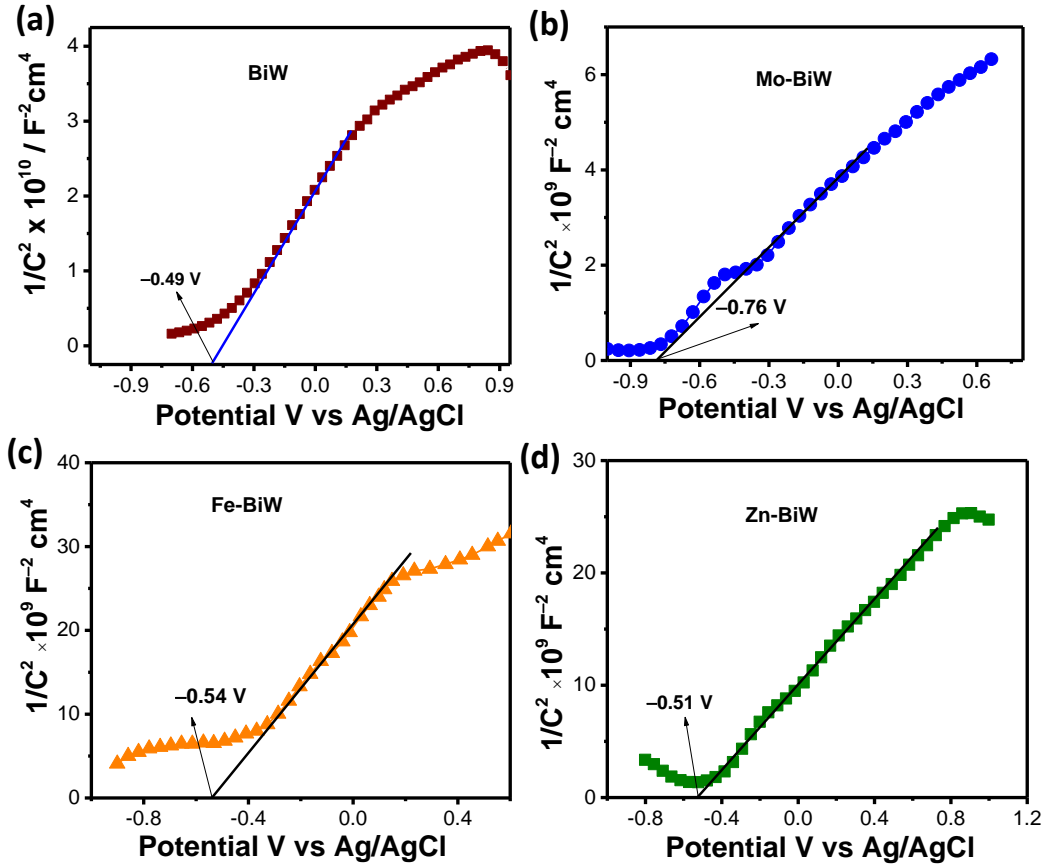


Figure 9 Mott-Schottky plots of (a) bare BiW, (b) Mo-BiW, (c) Fe-BiW and (d) Zn-BiW at frequency of 1000 Hz.

Table 2 Calculated Flat band potentials, CBM and VBM from the Mott-Schottky plots.

Material	E_{fb} V vs Ag/AgCl	E_{fb} V vs RHE	CBM eV	VBM eV	E_g eV
BiW	−0.49	0.12	−0.08	2.82	2.9
Mo-BiW	−0.76	−0.15	−0.35	2.19	2.54
Fe-BiW	−0.54	0.07	−0.13	2.64	2.77
Zn-BiW	−0.51	0.1	−0.1	2.72	2.82

Further, to validate the M-S results and understand the band alignment of the as developed materials, work function energies and the ionization potentials for the BiW and Mo-BiW were determined from the Secondary Electron Cutoff (SEC) and the valence band maxima (VBM) [59, 60]. Figure 10a represents the SEC spectra from where the secondary electron cutoff energies have been determined by the tangent at the linear portion of the spectra. The work function energies (ϕ) and the ionization potentials (IP) are presented in Table 3. It has been clearly observed that, after Mo-substitution the ϕ of Bi_2WO_6 decreases, which may be attributed to the enhancement of ion mobility [13]. More interestingly, the IP of Mo-BiW is less compared to the bare BiW, which strongly reveals the successful doping of Mo [13, 84].

Table 3 The secondary electron cutoff, work function energies, VBM position and ionization potential of the as developed materials.

Material	Secondary Electron Cutoff (SEC)	Work function energy (ϕ), eV	VBM position-eV	Ionization Potential (IP) eV
BiW	1482.05	4.55	2.82	7.37
Mo-BiW	1483	3.6	2.22	5.82

The valence band spectra for the BiW and Mo-BiW are shown in Figure 10b. The VBM energies were determined by fitting the tangent to the rising edge and its intersection with the background line. It is noted that there is a small density of states between the Fermi level (0 eV) and the band edge after Mo-doping. This is possibly due to unreacted Mo metal or presence of defects in the material [62]. A schematic band structures of bare BiW and Mo-BiW have been presented in Figure 10c, which are drawn based on the values of VBM, work function and ionization potential energies. The measurements show that the materials exhibit n-type conductivity, which is well consistent with the M-S measurement. Furthermore, Figure 10c illustrates that IP is pushed up by Mo doping, which facilitates the photocatalytic activity for water splitting.

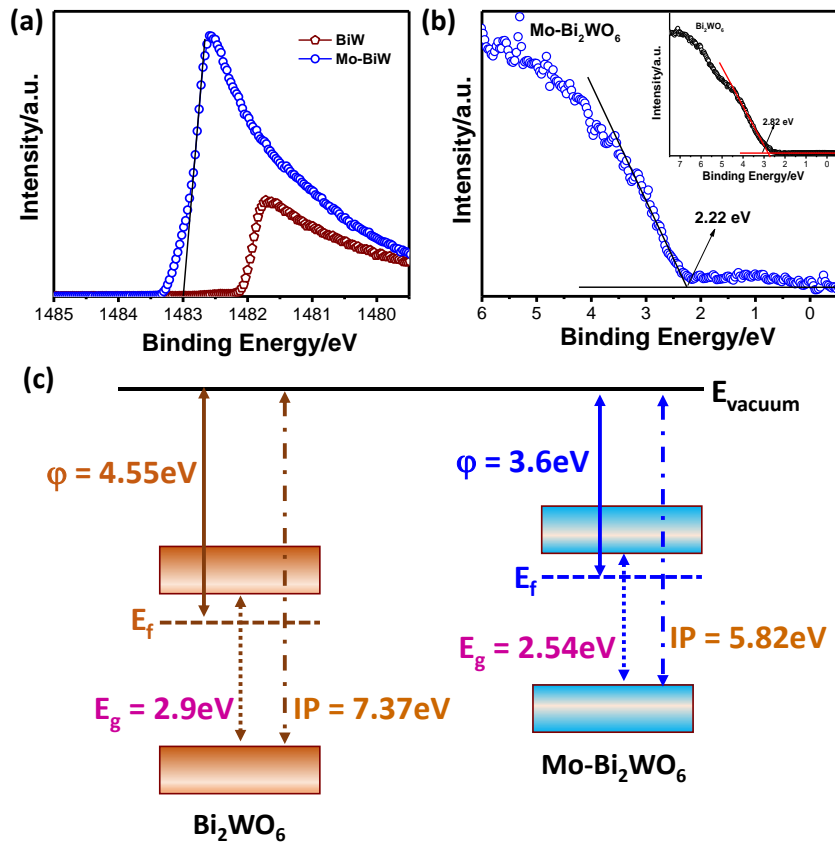


Figure 10 (a) Secondary Electron Cutoff (SEC) spectra of bare BiW and Mo-BiW. (b) The valence band maxima (VBM) spectra Mo-BiW. Inset: VBM of bare BiW. (c) Schematic Band structure of bare BiW and Mo-BiW.

4. Conclusions

In summary, a stable metal (Fe, Zn, Mo) doped Bi_2WO_6 double perovskite has been synthesized *via* one-pot hydrothermal method to achieve efficient charge separation under visible light irradiation. The doping of metals was confirmed from the XRD, EDX and (for Mo) XPS core level analysis. Among Mo, Fe, Zn doping, Mo-doped BiW showed superior catalytic activity in water splitting due to the synergistic effect of high mobility, higher number of free charge carriers and the reduced work function energy. Moreover, the lower ionization potential for Mo-BiW indicates improved charge separation and possibly electron mobility. The flat band potential for Mo-BiW shifted towards negative potential compared to that of bare BiW, indicating reduced onset potential which is related to low work function energy. As a result, fifty-seven times higher photocurrent density was achieved for Mo-BiW, compared to that from bare BiW. Thus, this study provides insight into the effect in metal doping in bandgap tuning and water splitting, thereby opening up an avenue for rational design of visible light active double perovskite-based photocatalyst.

Acknowledgments

The authors acknowledge Director, CSIR-CGCRI for her kind permission to publish this work. One of the authors (SB) is thankful to Department of Science & Technology (DST), India, for providing INSPIRE fellowship award and Newton Bhabha PhD Placement Award, (SS) is thankful to CSIR, India, for providing junior research fellowship award. SG acknowledges DST, India (project no. DST/TMD/MECSP/2K17/07), Science and Engineering Research Board (SERB) POWER Grant (project no. SPG/2020/000720) for financial support. VRD acknowledges support from the UK Engineering and Physical Sciences Research Council, (EP/J021229/1).

Conflict of Interest

The authors have declared no conflicts of interest for this article.

References

- [1] D. Ravelli, S. Protti, M. Fagnoni, A. Albini, Visible Light Photocatalysis. A Green Choice?. *Curr. Org. Chem.* 17 (2013) 2366–2373.
- [2] Q. Wang, K. Domen, Particulate Photocatalysts for Light-Driven Water Splitting: Mechanisms, Challenges, and Design Strategies. *Chem. Rev.* 120 (2020) 919–985.
- [3] S. Protti, M. Fagnoni, The sunny side of chemistry: green synthesis by solar light. *Photochem. Photobio. Sci.* 8 (2009) 1499–1516.
- [4] S. Banerjee, S. C. Pillai, P. Falaras, K. E. O’Shea, J. A. Byrne, D. D. Dionysiou, New Insights into the Mechanism of Visible Light Photocatalysis. *J. Phys. Chem. Lett.* 5 (2014) 2543–2554.
- [5] A. Listorti, J. Durrant, J. Barber, Solar to fuel. *Nat. Mater.* 8 (2009) 929–930.
- [6] A. Modak, K. Yamanaka, Y. Goto, S. Inagaki, Photocatalytic H₂ Evolution by Pt-Loaded 9,9’-Spirobifluorene-Based Conjugated Microporous Polymers under Visible-Light Irradiation. *Bull. Chem. Soc. Jpn.* 89 (2016) 887–891.
- [7] M. Grätzel, Photoelectrochemical cells. *Nature* 414 (1983) 338–344.
- [8] S. J. A. Moniz, S. A. Shevlin, D. J. Martin, Z.-X. Guo, J. Tang, Visible-light driven heterojunction photocatalysts for water splitting—a critical review. *Energy Environ. Sci.* 8 (2015) 731–759.
- [9] K. Sivula, R. V. D. Krol, Semiconducting materials for photoelectrochemical energy conversion. *Nat. Rev. Mater.* 1 (2016) 15010.

- [10] T. Takata, J. Jiang, Y. Sakata, M. Nakabayashi, N. Shibata, V. Nandal, K. Seki, T. Hisatomi, K. Domen, Photocatalytic water splitting with quantum efficiency of almost unity. *Nature* 581 (2020) 411–414.
- [11] Q. Wang, T. Hisatomi, Q. Jia, H. Tokudome, M. Zhong, C. Wang, Z. Pan, T. Takata, M. Nakabayashi, N. Shibata, Y. Li, I. D. Sharp, A. Kudo, T. Yamada, K. Domen, Scalable water splitting on particulate photocatalyst sheets with a solar-to-hydrogen energy conversion efficiency exceeding 1%. *Nat. Mater.* 15 (2016) 611–615.
- [12] J. Fu, Z. Fan, M. Nakabayashi, H. Ju, N. Pastukhova, Y. Xiao, C. Feng, N. Shibata, K. Domen, Y. Li, Interface engineering of Ta₃N₅ thin film photoanode for highly efficient photoelectrochemical water splitting. *Nat. Commun.* 13 (2022) 729–738.
- [13] K.-H. Ye, H. Li, D. Huang, S. Xiao, W. Qiu, M. Li, Y. Hu, W. Mai, H. Ji, S. Yang, Enhancing photoelectrochemical water splitting by combining work function tuning and heterojunction engineering *Nat. Commun.* 10 (2019) 3687–3696.
- [14] S. Bera, S. Ghosh, S. Shyamal, C. Bhattacharya, R. N. Basu, Photocatalytic hydrogen generation using gold decorated BiFeO₃ heterostructures as an efficient catalyst under visible light irradiation. *Sol. Energy Mater. Sol. Cells* 194 (2019) 195–206.
- [15] Y. Kuang, T. Yamada, K. Domen, Surface and interface engineering for photoelectrochemical water oxidation. *Joule* 1 (2017) 290–305.
- [16] M. Tomkiewicz, Scaling properties in photocatalysis. *Catal. Today* 58 (2000) 115–123.
- [17] G. Zhang, G. Liu, L. Wang, J. T. S. Irvine, Inorganic perovskite photocatalysts for solar energy utilization. *Chem. Soc. Rev.* 45 (2016) 5951–5984.

- [18] Y. W. Teh, M. K. T. Chee, X. Y. Kong, S.-T. Yong, S.-P. Chai, An insight into perovskite-based photocatalysts for artificial photosynthesis. *Sustainable Energy Fuels* 4 (2020) 973–984.
- [19] E. Vesali-Kermani, A. Habibi-Yangjeh, H. Diarmand-Khalilabad, S. Ghosh, Nitrogen photofixation ability of g-C₃N₄ nanosheets/Bi₂MoO₆ heterojunction photocatalyst under visible-light illumination. *J. Colloid Interface Sci.* 563 (2020) 81–91.
- [20] S. Bera, S. Ghosh, R. N. Basu, Fabrication of Bi₂S₃/ZnO heterostructures: an excellent photocatalyst for visible-light-driven hydrogen generation and photoelectrochemical properties. *New J. Chem.* 42 (2018) 541–554.
- [21] S. Shafafi, A. Habibi-Yangjeh, S. Feizpoor, S. Ghosh, T. Maiyalagan, Carbon dots and Bi₄O₅Br₂ adhered on TiO₂ nanoparticles: impressively boosted photocatalytic efficiency for removal of pollutants under visible light. *Sep. Purif. Technol.* 250 (2020) 117179.
- [22] S. Singh, A. Modak, K. K. Pant, A. Sinhamahapatra, P. Biswas, MoS₂–Nanosheets-Based Catalysts for Photocatalytic CO₂ Reduction: A Review. *ACS Appl. Nano Mater.* 4 (2021) 8644–8667.
- [23] A. Modak, A. K. Barui, C. R. Patra, A. Bhaumik, A luminescent nanoporous hybrid material based drug delivery system showing excellent theranostics potential for cancer. *Chem. Commun.* 49 (2013) 7644–7646.
- [24] H. Okudera, Y. Sakai, K. Yamagata, H. Takeda, Structure of russellite (Bi₂WO₆): origin of ferroelectricity and the effect of the stereoactive lone electron pair on the structure. *Acta Cryst. B* 74 (2018). 295–303.

- [25] H. C. Gupta, Archana, V. Luthra, Lattice dynamical investigations for Raman and infrared frequencies of Bi_2WO_6 . *J. Mol. Struct.* 1005 (2011) 53–58.
- [26] Z. Li, K. Wang, J. Zhang, Y. Chang, E. Kowalska, Z. Wei, Enhanced Photocatalytic Activity of Hierarchical Bi_2WO_6 Microballs by Modification with Noble Metals. *Catalysts* 12 (2022) 130–143.
- [27] W.-K. Jo, S. Kumar, S. Eslava, S. Tonda, Construction of $\text{Bi}_2\text{WO}_6/\text{RGO}/\text{g-C}_3\text{N}_4$ 2D/2D/2D hybrid Z-scheme heterojunctions with large interfacial contact area for efficient charge separation and high-performance photoreduction of CO_2 and H_2O into solar fuels. *Appl. Catal. B* 239 (2018) 586–598.
- [28] A. Kudo, S. Hiji, H_2 or O_2 Evolution from Aqueous Solutions on Layered Oxide Photocatalysts Consisting of Bi^{3+} with $6s^2$ Configuration and d^0 Transition Metal Ions. *Chem. Lett.* 10 (1999) 1103–1104.
- [29] Y. Zhou, Y. Zhang, M. Lin, J. Long, Z. Zhang, H. Lin, J. C.-S. Wu, X. Wang, Monolayered Bi_2WO_6 nanosheets mimicking heterojunction interface with open surfaces for photocatalysis. *Nat. Commun.* 6 (2015) 8340–8349.
- [30] T. Saison, P. Gras, N. Chemin, C. Chanéac, O. Durupthy, V. Brezová, C. Colbeau-Justin, J.-P. Jolivet, New insights into Bi_2WO_6 properties as a visible-light photocatalyst, *J. Phys. Chem. C* 117 (2013) 22656–22666.
- [31] S. G. Kumar, K. Koteswara Rao, Tungsten-based nanomaterials (WO_3 & Bi_2WO_6): Modifications related to charge carrier transfer mechanisms and photocatalytic applications, *Appl. Surf. Sci.* 355 (2015) 939–958.

- [32] A. Khlyustova, N. Sirotkin, T. Kusova, A. Kraev, V. Titov, A. Agafonov, Doped TiO₂: the effect of doping elements on photocatalytic activity. *Mater. Adv.* 1 (2020) 1193–1201.
- [33] S. S. Mohtar, F. Aziz, A. F. Ismail, N. S. Sambudi, H. Abdullah, A. N. Rosli, B. Ohtani, Impact of Doping and Additive Applications on Photocatalyst Textural Properties in Removing Organic Pollutants: A Review. *Catalysts* 11 (2021) 1160.
- [34] M. R. D. Khaki, M. S. Shafeeyan, A. A. A. Raman, W. M. A. W. Daud, Application of doped photocatalysts for organic pollutant degradation - A review. *J. Environ. Manag.* 198, (2017) 78–94.
- [35] Y. Zhang, Y. Zhao, Z. Xiong, T. Gao, B. Gong, P. Liu, J. Liu, J. Zhang, Elemental mercury removal by Γ -doped Bi₂WO₆ with remarkable visible light-driven photocatalytic oxidation. *Appl. Catal. B* 282 (2021) 119534.
- [36] L. Zhang, Y. Man, Y. Zhu, Effects of Mo Replacement on the Structure and Visible-Light-Induced Photocatalytic Performances of Bi₂WO₆ Photocatalyst. *ACS Catal.* 1 (2011) 841–848.
- [37] N. Tian, Y. Zhang, H. Huang, Y. He, Y. Guo, Influences of Gd substitution on the crystal structure and visble-light-driven photocatalytic performance of Bi₂WO₆, *J. Phys. Chem. C* 118 (2014) 15640–15648.
- [38] R. Shi, G. Huang, J. Lin, Y. Zhu, Photocatalytic activity enhancement for Bi₂WO₆ by fluorine substitution, *J. Phys. Chem. C* 113 (2009) 19633–19638.
- [39] Y. Wei, X. Wei, S. Guo, Y. Huang, G. Zhu, J. Zhang, The effects of Br dopant on the photo-catalytic properties of Bi₂WO₆, *Mater. Sci. Eng., B* 206 (2016) 79–84.

- [40] A. H. Ahsaine, A. Eljaouhari, A. Slassi, M. Ezahri, A. Benlhachemi, B. Bakiz, F. Guinneton, J. R. Gavarri, Electronic band structure and visible-light photocatalytic activity of Bi_2WO_6 : elucidating the effect of lutetium doping, *RSC Adv.* 6 (2016) 101105–101114.
- [41] R. Chen, C. H. Hu, S. Wei, J. H. Xia, J. Cui, H. Y. Zhou, Synthesis and activity of Agdoped Bi_2WO_6 photocatalysts, in: *Energy and Environment Materials*, Materials Science Forum, Trans Tech Publications Ltd 743 (2013) 560–566.
- [42] J. Wang, X. Gao, F. Fu, L. Zhang, Y. Wu, Photocatalytic degradation of phenolcontaining wastewater over $\text{Cu-Bi}_2\text{WO}_6$ composite under visible light irradiation, *J. Residuals Sci. Technol.* 9 (2012) 101–106.
- [43] Z. Zhang, W. Wang, E. Gao, M. Shang, J. Xu, Enhanced photocatalytic activity of Bi_2WO_6 with oxygen vacancies by zirconium doping, *J. Hazard. Mater.* 196 (2011) 255–262.
- [44] Y. Su, G. Tan, C. Xu, T. Liu, Y. Wang, H. Ren, A. Xia, The up-conversion effect induced NIR-photocatalytic performance of $\text{Bi}_{2-x}\text{Er}_x\text{WO}_6$ photocatalysts, *Mater. Lett.* 211 (2018) 175–178.
- [45] R. M. Mohamed, E. S. Aazam, Enhancement of photocatalytic properties of Bi_2WO_6 nanoparticles by Pt deposition, *Mater. Res. Bull.* 48 (2013) 3572–3578.
- [46] Y. Liu, W. Wang, Z. Fu, H. Wang, Y. Wang, J. Zhang, Nest-like structures of Sr doped Bi_2WO_6 : synthesis and enhanced photocatalytic properties, *Mater. Sci. Eng., B* 176 (2011) 1264–1270.

- [47] X. C. Song, W. T. Li, W. Z. Huang, H. Zhou, H. Y. Yin, Y. F. Zheng, Enhanced photocatalytic activity of cadmium-doped Bi_2WO_6 nanoparticles under simulated solar light, *J. Nanopart. Res.* 17 (2015) 134.
- [48] X. Xu, Y. Ge, B. Li, F. Fan, F. Wang, Shape evolution of Eu-doped Bi_2WO_6 and their photocatalytic properties, *Mater. Res. Bull.* 59 (2014) 329–336.
- [49] W. T. Li, W. Z. Huang, H. Zhou, H. Y. Yin, Y. F. Zheng, X. C. Song, Synthesis and photoactivity enhancement of Ba doped Bi_2WO_6 photocatalyst, *Mater. Res. Bull.* 64 (2015) 432–437.
- [50] K. Lai, Y. Zhu, J. Lu, Y. Dai, B. Huang, N- and Mo-doping Bi_2WO_6 in photocatalytic water splitting, *Comput. Mater. Sci.* 67 (2013) 88–92.
- [51] Y. Zhang, Y. Ma, Q. Liu, H. Jiang, Q. Wang, D. Qu, J. Shi, Synthesis of $\text{Er}^{3+}/\text{Zn}^{2+}$ co-doped Bi_2WO_6 with highly efficient photocatalytic performance under natural indoor weak light illumination, *Ceram. Int.* 43 (2017) 2598–2605.
- [52] X. Meng, H. Qin, Z. Zhang, New Insight into the Enhanced Visible Light-Driven Photocatalytic Activity of Pd/PdCl₂-doped Bi_2WO_6 Photocatalysts. *J. Colloid Interface Sci.* 513, 1 (2018) 877–890.
- [53] J. Huang, G. Q. Tan, H. J. Ren, A. Xia, Y. Y. Luo, Multi-factors on photocatalytic properties of Y-doped Bi_2WO_6 crystallites prepared by microwave-hydrothermal method. *Cryst. Res. Technol.* 49 (2014) 467.
- [54] M. Wang, Z. Y. Qiao, M. H. Fang, Z. H. Huang, Y. G. Liu, X. W. Wu, C. Tang, H. Tang, H. K. Zhu, Synthesis of Er-doped Bi_2WO_6 and enhancement in photocatalytic activity induced by visible light. *RSC Adv.* 5 (2015) 94887.

- [55] H. W. Huang, K. Liu, K. Chen, Y. L. Zhang, Y. H. Zhang, S. C. Wang, Ce and F Comodification on the Crystal Structure and Enhanced Photocatalytic Activity of Bi_2WO_6 Photocatalyst under Visible Light Irradiation. *J. Phys. Chem. C* 118 (2014) 14379.
- [56] S. Guo, X. Li, H. Wang, F. Dong, Z. Wu, Fe-ions modified mesoporous Bi_2WO_6 nanosheets with high visible light photocatalytic activity, *J. Colloid Interface Sci.* 369 (2012) 373–380.
- [57] C. Bhattacharya, H. C. Lee, A. J. Bard, Rapid Screening by Scanning Electrochemical Microscopy (SECM) of Dopants for Bi_2WO_6 Improved Photocatalytic Water Oxidation with Zn Doping. *J. Phys. Chem. C* 117 (2013) 9633–9640.
- [58] A. Etogo, R. Liu, J. Ren, L. Qi, C. Zheng, J. Ning, Y. Zhong, Y. Hu, Facile one-pot solvothermal preparation of Mo doped Bi_2WO_6 biscuit-like microstructures for visible-light-driven photocatalytic water oxidation. *J. Mater. Chem. A* 4 (2016) 13242–13250.
- [59] S. P. Keerthana, B. J. Rani, G. Ravi, R. Yuvakkumar, S. I. Hong, D. Velauthapillai, B. Saravanakumar, M. Thambidurai, C. Dang, Ni doped Bi_2WO_6 for electrochemical OER activity. *Int. J. Hydrogen Energy* 45 (2020) 18859–18866.
- [60] V. Koteski, J. Belošević-Čavor, V. Ivanovski, A. Umićević, D. Toprek, Abinitio calculations of the optical and electronic properties of Bi_2WO_6 doped with Mo, Cr, Fe, and Zn on the W-lattice site. *Appl. Surface Sci.* 515 (2020) 146036–146042.
- [61] T. J. Whittles, T. D. Veal, C. N. Savory, P. J. Yates, P. A. E. Murgatroyd, J. T. Gibbon, M. Birkett, R. J. Potter, J. D. Major, K. Durose, D. O. Scanlon, V. R. Dhanak, Band Alignments, Band Gap, Core Levels, and Valence Band States in Cu_3BiS_3 for Photovoltaics. *ACS Appl. Mater. Interfaces* 11 (2019) 27033–27047.

- [62] T. J. Whittles, L. A. Burton, J. M. Skelton, A. Walsh, T. D. Veal, V. R. Dhanak, Band Alignments, Valence Bands, and Core Levels in the Tin Sulfides SnS, SnS₂, and Sn₂S₃: Experiment and Theory. *Chem. Mater.* 28 (2016) 3718–3726.
- [63] A. N. Mallika, A. R. Reddy, K. S. Babu, C. Sujatha, K. V. Reddy, Structural and photoluminescence properties of Mg substituted ZnO nanoparticles. *Optical Mater.* 36 (2014) 879–884.
- [64] A. Sa'aedi, A. A. Akl, A. S. Hassanien, Effective role of Rb doping in controlling the crystallization, crystal imperfections, and microstructural and morphological features of ZnO-NPs synthesized by the sol–gel approach. *Cryst. Eng. Comm.* 24 (2022) 4661–4678.
- [65] R. Mariappan, V. Ponnuswamy, P. Suresh, Effect of doping concentration on the structural and optical properties of pure and tin doped zinc oxide thin films by nebulizer spray pyrolysis (NSP) technique. *Superlattices Microstruct.* 52 (2012) 500–513.
- [66] D. K. Chanda, D. Mukherjee, P. S. Das, C. K. Ghosh, A. K. Mukhopadhyay, Novel Growth Mechanisms of Self-assembled Mg(OH)₂ Nanoplatelets. *Trans. Ind. Ceram. Soc.* 77 (2018) 235–243.
- [67] S. Ghosh, S. Bera, A. Singh, S. Basu, R. N. Basu, Hierarchical Bi₂WO₆/BiFeWO₆ n-n heterojunction as an efficient photocatalyst for water splitting under visible light. *J. Alloys Compd.* 919 (2022) 165700.
- [68] S. Bera, S. Ghosh, T. Maiyalagan, R. N. Basu, Band Edge Engineering of BiOX/CuFe₂O₄ Heterostructures for Efficient Water Splitting. *ACS Appl. Energy Mater.* 5 (2022) 3821–3833.

- [69] P. Morandi, V. Flaud, S. Tingry, D. Cornu, Y. Holade, Tartaric acid regulated the advanced synthesis of bismuth-based materials with tunable performance towards the electrocatalytic production of hydrogen peroxide. *J. Mater. Chem. A* 8 (2020) 18840–18855.
- [70] R. Levinas, N. Tsyntsaru, T. Murauskas, H. Cesiulis, Improved Photocatalytic Water Splitting Activity of Highly Porous WO_3 Photoanodes by Electrochemical H^+ Intercalation. *Front. Chem. Eng.* 3 (2021) 760700–760717.
- [71] Y. Lv, W. Yao, R. Zong, Y. Zhu, Fabrication of Wide-Range-Visible Photocatalyst $\text{Bi}_2\text{WO}_{6-x}$ nanoplates via Surface Oxygen Vacancies. *Sci. Rep.* 6 (2016) 19347–19357.
- [72] J. S. Cho, Large Scale Process for Low Crystalline MoO_3 -Carbon Composite Microspheres Prepared by One-Step Spray Pyrolysis for Anodes in Lithium-Ion Batteries. *Nanomaterials* 9 (2019) 539–551.
- [73] F. Xie, W. C. H. Choy, C. Wang, X. Li, S. Zhang, J. Hou, Low-Temperature Solution-Processed Hydrogen Molybdenum and Vanadium Bronzes for an Efficient Hole-Transport Layer in Organic Electronics. *Adv. Mater.* 25 (2013) 2051–2055.
- [74] M. A. Bica de Moraes, B. C. Trasferetti, F. P. Rouxinol, R. Landers, S. F. Durrant, J. Scarmínio, A. Urbano, Molybdenum oxide thin films obtained by the hot-filament metal oxide deposition technique. *Chem. Mater.* 16 (2003) 513–520.
- [75] J. Huang, X. Li, G. Su, R. Gao, W. Wang, B. Dong, L. Cao, Construction of layer-by-layer $\text{g-C}_3\text{N}_4/\text{Ag}/\text{Bi}_2\text{WO}_6$ Z-scheme system with enhanced photocatalytic activity. *J. Mater. Sci.* 53 (2018) 16010–16021.

- [76] A. Kaur, S. Kansal, Bi₂WO₆ nanocuboids: An efficient visible light active photocatalyst for the degradation of levofloxacin drug in aqueous phase. *Chem. Eng. J.* 302 (2016) 194.
- [77] P. Makuła, M. Pacia, W. Macyk, How To Correctly Determine the Band Gap Energy of Modified Semiconductor Photocatalysts Based on UV–Vis Spectra. *J. Phys. Chem. Lett.* 9 (2018) 6814–6817.
- [78] T. Hu, H. Li, N. Du, W. Hou, Iron-Doped Bismuth Tungstate with an Excellent Photocatalytic Performance. *Chem. Cat. Chem.*, 2018, 10, 3040–3048.
- [79] V. L. Ranganatha, S. Pramila, G. Nagaraju, B. S. Surendra, C. Mallikarjunaswamy J. *Mater. Sci.* 31 (2020) 1.
- [80] R. van de Krol, A. Goossens, J. Schoonman, Mott-Schottky Analysis of Nanometer-Scale Thin-Film Anatase TiO₂. *J. Electrochem. Soc.* 144 (1997) 1723.
- [81] L. Liu, Y. Qi, J. Lu, S. Lin, W. An, J. Hu, Y. Liang, W. Cui, Dramatic activity of a Bi₂WO₆@g-C₃N₄ photocatalyst with a core@shell structure. *RSC Adv.* 5 (2015) 99339–99346.
- [82] J. Li, H. Hao, J. Zhou, Z. Zhu, g-C₃N₄ modified flower-like WO₃–Bi₂WO₆ microspheres with enhanced photoelectrocatalytic activity. *New J. Chem.* 40 (2016) 9638–9647.
- [83] Y. Matsumoto, Energy Positions of Oxide Semiconductors and Photocatalysis with Iron Complex Oxides. *J. Solid State Chem.* 126 (1996) 227–234.
- [84] P. Biswas, A. Ainabayev, A. Zhussupbekova, F. Jose, R. O'Connor, A. Kaisha, B. Walls, I. V. Shvets, Tuning of oxygen vacancy-induced electrical conductivity in Ti-doped hematite films and its impact on photoelectrochemical water splitting. *Sci. Rep.* 10 (2020) 7463–7472.

Supporting Information

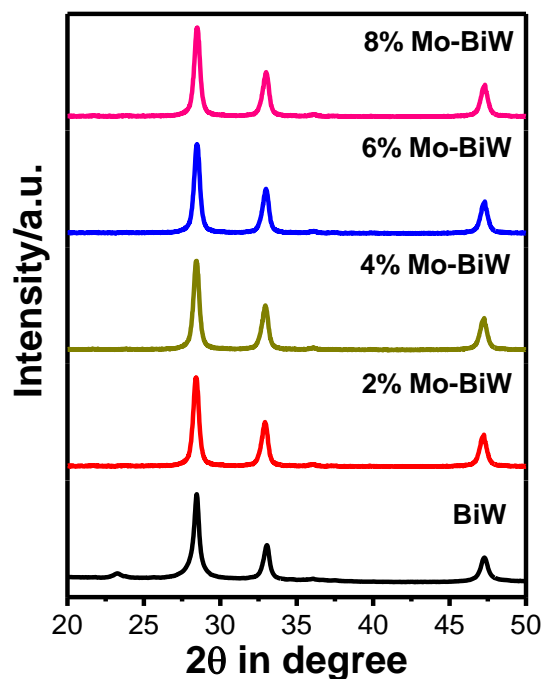


Figure S1 XRD patterns of bare BiW and Mo-BiW at different percentage of Mo doping.

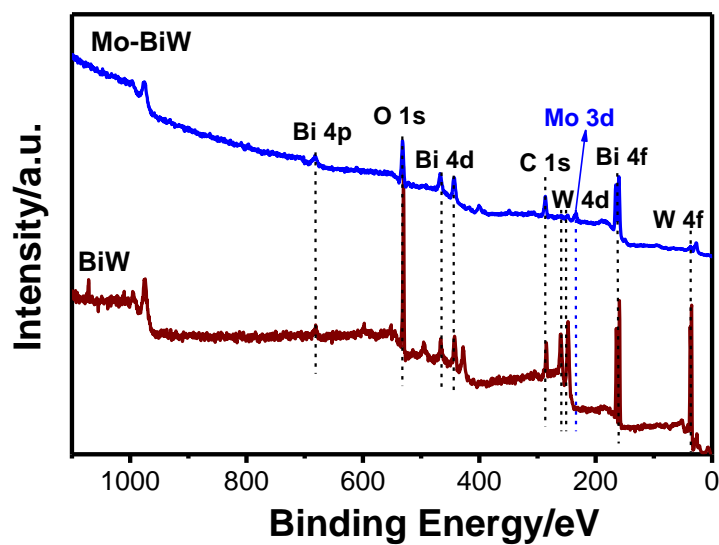


Figure S2 Surface survey XPS spectra of bare BiW and 6% Mo-BiW.

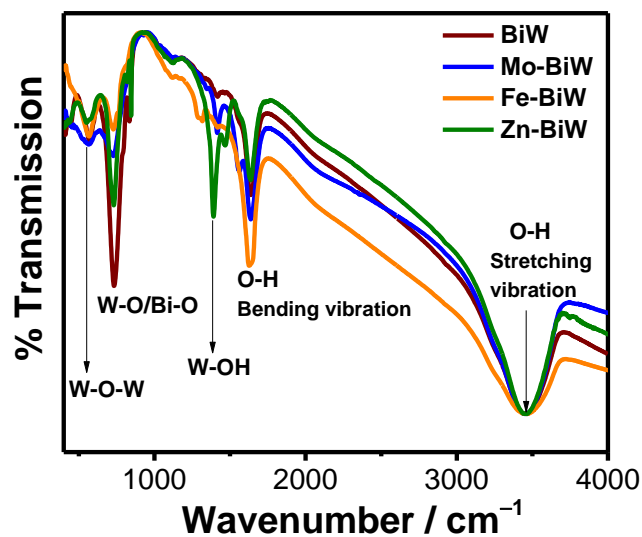


Figure S3 FTIR spectra of pristine Bi_2WO_6 and 6% metal-doped (Mo, Fe, Zn) Bi_2WO_6 .

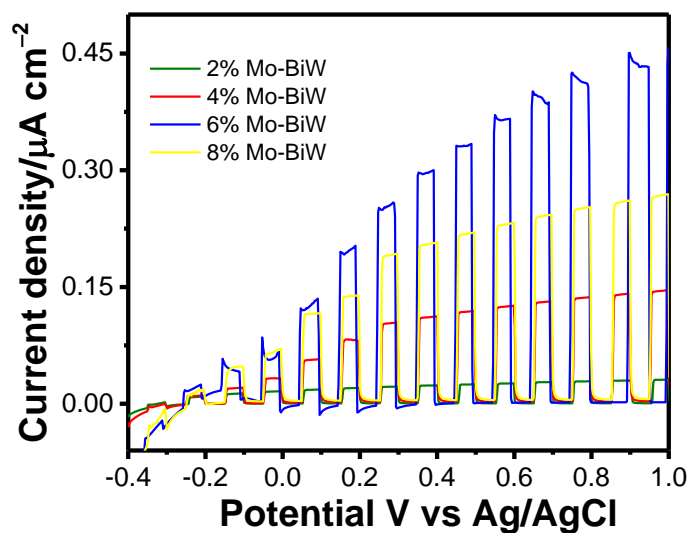


Figure S4 Chopped LSV spectra of Mo doped BiW with different dopant percentage.

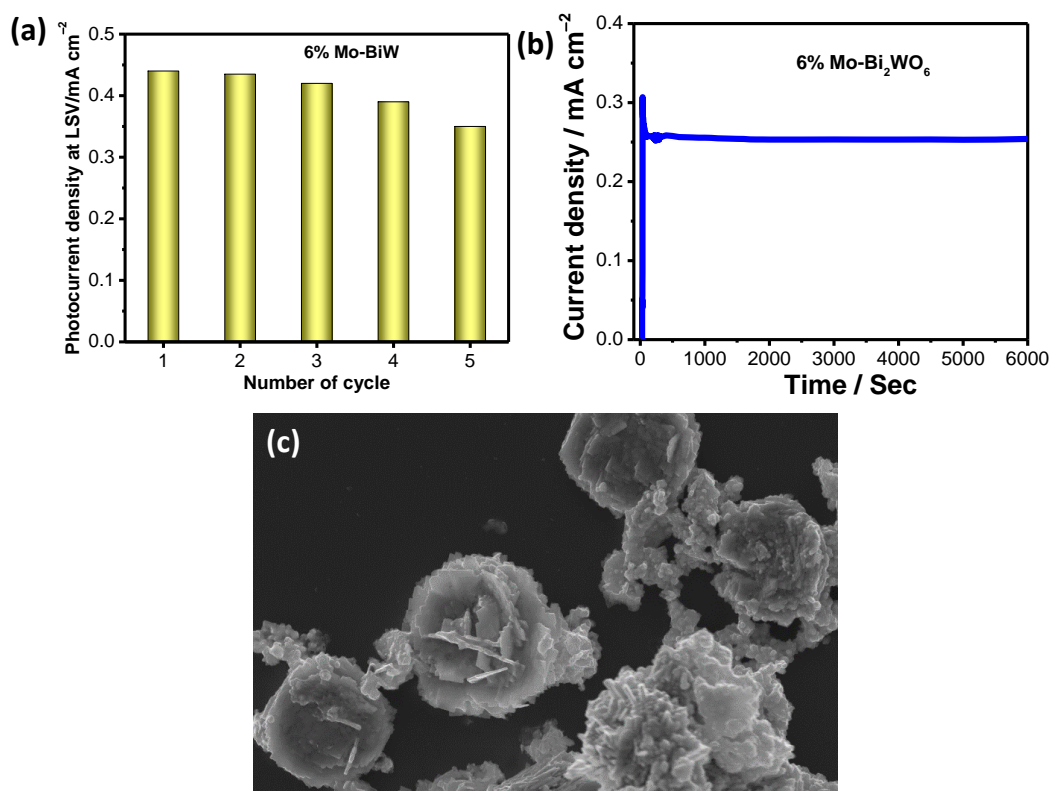


Figure S5 (a) Successive LSV scans and (b) chronoamperometry spectra of Mo-doped Bi₂WO₆ under continuous visible light illumination. (c) FESEM image of Mo-doped Bi₂WO₆ after ten successive LSV scans.

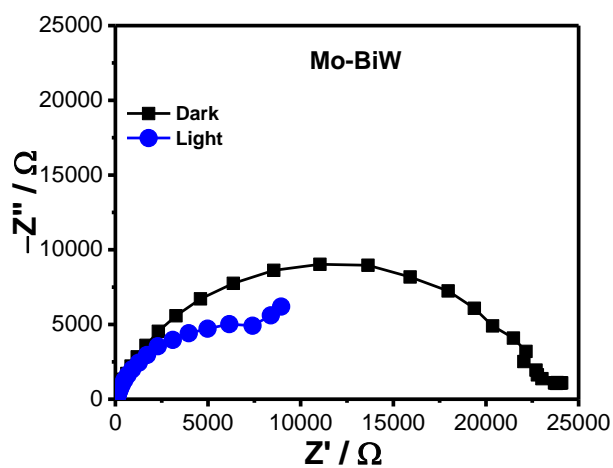


Figure S6 Nyquist plot of 6% Mo-BiW at 0.26 V vs Ag/AgCl in 0.1 M Na₂SO₄ electrolyte under dark and visible light illumination.

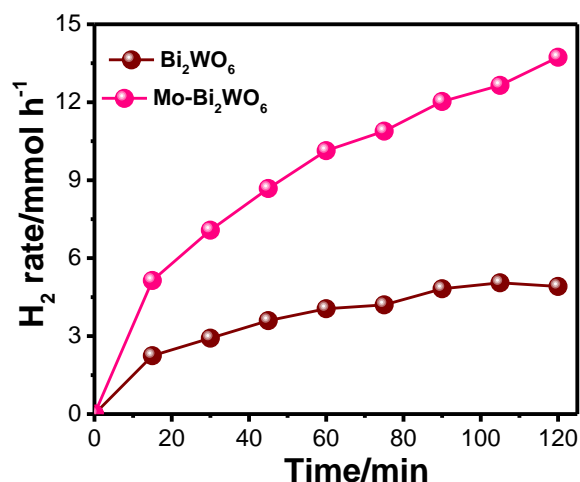


Figure S7 Photocatalytic H₂ generation using pristine Bi₂WO₆ and Mo-doped Bi₂WO₆.

Table S1 Comparative table of doped Bi₂WO₆ and Bi₂WO₆-based heterostructures used for various photocatalytic applications.

Material	Photocatalytic Activity	Performance	Reference
2D Bi ₂ WO ₆	Photocatalytic H ₂ generation	56.9 μmol/g/h	3
(001)-Bi ₂ WO ₆	PEC Water splitting	150 μA/cm ² photo-current density	15
Monolayer Bi ₂ WO ₆	Photocatalytic H ₂ generation	16 μmol/g	17
Bi ₂ WO ₆ nano flower	Photocatalytic H ₂ generation	11 mmol	18
Bismuth vacancy mediated single unit cell Bi ₂ WO ₆	Photocatalytic O ₂ generation	110 μmol/g/h	20
Cu-doped Bi ₂ WO ₆	Photocatalytic degradation of NOF	89.27% activity	30
Pd/PdCl ₂ -doped Bi ₂ WO ₆	phenol degradation	98% efficiency in 40 min	40
I ⁻ -doped Bi ₂ WO ₆	gas-phase elemental mercury removal	87.6 % removal efficiency	41
Zr ⁴⁺ -doped Bi ₂ WO ₆	photodegradation of rhodamine B (RhB)	100% degradation in 20 min	31
Boron doped Bi ₂ WO ₆	photodegradation of RhB	100% degradation in 180 min	37
Mg, Fe, Zn and Cu doped- Bi ₂ WO ₆	NOR and CIP removal	1% Mg/Bi ₂ WO ₆ exhibited the highest degradation rate of 89.44% for NOR and 99.11% for CIP	28
Er-doped Bi ₂ WO ₆	degradation of RhB	99% in 4h	44
Iron-Doped Bismuth Tungstate	degradation of RhB	93% in 7h	56
Mo-doped Bi ₂ WO ₆	degradation of RhB	0.045 min ⁻¹	24

Sm-doped Bi ₂ WO ₆	degradation of RhB	98.4% removal rate within 30 min	34
Mo-doped Bi ₂ WO ₆	O ₂ evolution	147.2 $\mu\text{mol h}^{-1}\text{g}^{-1}$ 3.1% apparent quantum efficiency at 420nm	48
Ni doped Bi ₂ WO ₆	electrochemical OER activity	272 mA/g	50
Zn-doped Bi ₂ WO ₆	PEC water splitting	0.1 mA cm ⁻²	42
Carbon quantum dot decorated Bi ₂ WO ₆	CO ₂ reduction	CH ₄ , CO production	a
g-C ₃ N ₄ /Bi ₂ WO ₆	decomposition of TC and RhB under visible light	90% degradation	b
2D Bi ₂ WO ₆	Photocatalytic H ₂ generation	56.9 $\mu\text{mol/g/h}$	c
Bi/g-C ₃ N ₄ /Bi ₂ WO ₆	Photocatalytic MO and RhB degradation	80% degradation	d
Bi ₂ Fe ₄ O ₉ /Bi ₂ WO ₆	Photodegradation of RhB	99 % degradation	e
CdS/Ag/Bi ₂ MoO ₆	photocatalytic decolorization of RhB aqueous solution under visible light	98% degradation	f
ZnMoO ₄ /BiFeWO ₆ /RGO	degradation of AB 25	80 % degradation	g
ZnIn ₂ S ₄ /Bi ₂ WO ₆	decomposition of aqueous metronidazole (MTZ) under visible-light irradiation	96% degradation	h
AgBr/Bi ₂ WO ₆	Photocatalytic degradation of methylene blue	92% degradation	i
Ag/Bi ₂ WO ₆	Photocatalytic degradation of phenol	99 % degradation	j
Bi ₂ WO ₆ -Cu ₃ P	Water splitting	8 $\mu\text{mol/g}$, H ₂ 4 $\mu\text{mol/g}$, O ₂	k
RGO-Bi ₂ WO ₆	Photocatalytic H ₂ generation	6 mmol	l
Bi ₂ WO ₆ nano flower	Photocatalytic H ₂ generation	11 mmol	m
Bi ₂ WO ₆ /RGO/g-C ₃ N ₄	Water splitting	0.55 μmol , H ₂ 2.55 μmol , O ₂	n
(001)-Bi ₂ WO ₆	PEC Water splitting	150 $\mu\text{A/cm}^2$ photo-current density	o
Ag ₃ PO ₄ /Bi ₂ WO ₆	degradation of phenol	98% degradation	p
Monolayer Bi ₂ WO ₆	Photocatalytic H ₂ generation	16 $\mu\text{mol/g}$	q
Mo, Fe, Zn-doped Bi₂WO₆	PEC water splitting	0.4 mA cm⁻² for Mo-Bi₂WO₆ 0.17 mA cm⁻² for Fe-Bi₂WO₆ 8.49 $\mu\text{A cm}^{-2}$ for Fe-Bi₂WO₆ 7.07 $\mu\text{A cm}^{-2}$ for Bi₂WO₆	Present work

References:

- a) X. Y. Kong, W. L. Tan, B.-J. Ng, S.-P. Chai and A. R. Mohamed, *Nano Res.*, 2017, **10**, 1720–1731.
- b) X. Zhu, J. Liu, Z. Zhao, J. Yan, Y. Xu, Y. Song, H. Ji, H. Xu and H. Li, *RSC Adv.*, 2017, **7**, 38682–38690.
- c) S. Wu, J. Sun, Q. Li, Z. D. Hood, S. Yang, T. Su, R. Peng, Z. Wu, W. Sun, P. R. C. Kent, B. Jiang and M. F. Chisholm, *ACS Appl. Mater. Interfaces*, 2020, **12**, 20067–20074.
- d) J. Wang, L. Tang, G. Zeng, Y. Liu, Y. Zhou, Y. Deng, J. Wang and B. Peng, *ACS Sustainable Chem. Eng.*, 2017, **5**, 1062–1072.
- e) B. Li, C. Lai, G. Zeng, L. Qin, H. Yi, D. Huang, C. Zhou, X. Liu, M. Cheng, P. Xu, C. Zhang, F. Huang and S. Liu, *ACS Appl. Mater. Interfaces*, 2018, **10**, 18824–18836.
- f) D. Wang, H. Shen, L. Guo, F. Fu and Y. Liang, *New J. Chem.*, 2016, **40**, 8614–8624.
- g) P. J. Mafa, B. Ntsendwana, B. B. Mamba and A. T. Kuvarega, *J. Phys. Chem. C*, 2019, **123**, 20605–20616.
- h) W.-K. Jo, J. Y. Lee and T. S. Natarajan, *Phys. Chem. Chem. Phys.*, 2016, **18**, 1000–1016.
- i) D. Wang, L. Guo, Y. Zhen, L. Yue, G. Xue and F. Fu, *J. Mater. Chem. A*, 2014, **2**, 11716–11727.
- j) Z. Zhang, W. Wang, E. Gao, S. Sun and L. Zhang, *J. Phys. Chem. C*, 2012, **116**, 25898–25903.
- k) A. Rauf, M. Ming, S. Kim, S. A. S. Shah, C.-H. Chung, J. Hyeok, Park and P. J. Yoo, *Nanoscale*, 2018, **10**, 3026–3036.
- l) J. Zhao, Y. Yang, X. Dong, Q. Ma, W. Yu, J. Wang and G. Liu, *RSC Adv.*, 2016, **6**, 64741–64748.
- m) R. P. Panmand, Y. A. Sethi, S. R. Kadam, M. S. Tamboli, L. K. Nikam, J. D. Ambekar, C.-J. Park and B. B. Kale, *Cryst. Eng. Comm.*, 2015, **17**, 107–115.
- n) W.-K. Jo, S. Kumar, S. Eslav, S. Tonda, *Appl. Catal. B*, 2018, **239**, 586–598.
- o) R. Ullah, M. Pei, J. Wu, Y. Tian, Z. Gu, Q. Zhang, C. Song, Y. Yang, M. Ahmad, J. Zeb, F. Qayyum, Y. Liu, X. An, L. Gu, X. Wang and J. Zhang, *ACS Appl. Energy Mater.*, 2020, **3**, 4149–4154.
- p) G. Fu, G. Xu, S. Chen, L. Lei and M. Zhang, *Catal. Commun.*, 2013, **40**, 120–124.
- q) Y. Zhou, Y. Zhang, M. Lin, J. Long, Z. Zhang, H. Lin, J. C.-S. Wu and X. Wang, *Nat. Commun.*, 2016, **6**, 8340–8348.